

# Laplace-Beltrami Operator for Gaussian Splatting

Hongyu Zhou<sup>1,2</sup>

Zorah Löhner<sup>1,2</sup>

<sup>1</sup>University of Bonn

<sup>2</sup>Lamarr Institute

hzhou, laehner@uni-bonn.de

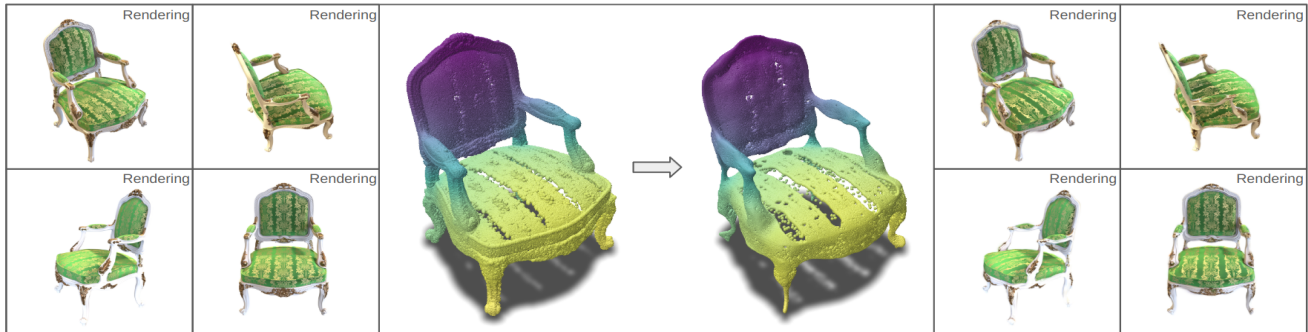


Figure 1. We introduce a novel method to accurately compute the Laplace-Beltrami operator directly on 3D Gaussian splats, leveraging both the center and the covariance information. The operator can be directly applied on 3D Gaussian splats, without the need for mesh extraction, for multiple applications such as surface smoothing, as shown above. We can transform the original scene (left) by computing the Laplace-Beltrami eigenfunctions (middle, both original and smoothed), leading to a smoothed scene of the 3D Gaussians splats (right), which presents transformation on the original rendering (left) and the computed Laplace-Beltrami eigenfunction (middle).

## Abstract

*With the rising popularity of 3D Gaussian splatting and the expanse of applications from rendering to 3D reconstruction, there comes also a need for geometry processing applications directly on this new representation. While considering the centers of Gaussians as a point cloud or meshing them is an option that allows to apply existing algorithms, this might ignore information present in the data or be unnecessarily expensive. Additionally, Gaussian splatting tends to contain a large number of outliers which do not affect the rendering quality but need to be handled correctly in order not to produce noisy results in geometry processing applications. In this work, we propose a formulation to compute the Laplace-Beltrami operator, a widely used tool in geometry processing, directly on Gaussian splatting using the Mahalanobis distance. While conceptually similar to a point cloud Laplacian, our experiments show superior accuracy on the point clouds encoded in the Gaussian splatting centers and, additionally, the operator can be used to evaluate the quality of the output during optimization. Our code will be released on github soon.*

## 1. Introduction

3D Gaussian Splatting (3DGS) [19] has recently revolutionized 3D scene representations. By representing complex scenes as a set of 3D Gaussians, it achieves photorealistic results for novel view synthesis while allowing much more efficient training and real-time rendering compared to NeRF based approaches [2]. Even though it was originally proposed for rendering applications, it is now also popular as a general 3D representation [14, 16]. However, due to its initial focus on rendering, most 3DGS methods do not lead to an accurate surface representation. To overcome this, a series of work has been produced with a focus on surface reconstruction instead [10, 16]. One possibility is to pull the 3D Gaussians to the suspected surface and then reconstruct a mesh via Poisson reconstruction [15, 18]. Another approach was suggested in [16] by restricting the Gaussians to be 2D which leads to more accurate surface mappings (as the surface of a 3D object is a 2D manifold).

As the geometric reconstruction accuracy advances, the need for common geometry processing tools directly on this representation rises. For example, manual editing through deformation energies [17] and semantic segmentation [8]

have been proposed for Gaussian splatting. In this paper we will look at the Laplace-Beltrami operator (LBO), which is often called the "Swiss Army knife" of geometry processing and used in a wide variety of geometry processing applications [22, 30, 33]. One core information in the LBO is the connectivity between points which is not explicitly included in Gaussian splatting. It is possible to consider the 3DGS as a point cloud by taking the set of Gaussian centers, however, this ignores a lot of information included in the variances and generally does not work well due to the high density of outliers in Gaussian splatting. The outliers stem from the optimization from images, which normally do not depict the inside of objects. Additionally, low opacity Gaussians do not significantly change the appearance but stay present in the point cloud of centers. We propose to compute the Laplace-Beltrami operator by using the Mahalanobis distance which can leverage the variance of the Gaussians as an indicator of surface direction. To show the performance of the LBO, we experiment on classical geometry processing applications such as distance computation and shape matching.

**Contributions.** Our contributions are as follows:

1. The definition of a Laplace-Beltrami operator that can be computed directly on Gaussian splatting and takes into account all information encoded by the variance.
2. We show a relationship between the eigenvalues of the LBO and stable geometry of 3DGS, and how they can be used to determine convergence during optimization.
3. We experimentally demonstrate the effectiveness of this LBO on a variety of geometry processing applications.

In addition, we will publish a variation of the popular geometry processing dataset [6], in which we generated renderings and 3D Gaussian splatting reconstructions of all shapes, including correspondences between both, to facilitate further research on geometry processing applications using 3DGS.

## 2. Related Work

In this section, we show connections to the most relevant related work. A broader introduction into Gaussian splatting can be found in the survey of [9].

### 2.1. Gaussian Splatting

3D Gaussian splatting was introduced in [19] as an efficient framework for novel-view synthesis. It optimizes over a set of Gaussian distributions in 3D space with color and opacity values which can be rendered from new view points. While this works exceptionally well and has been applied to many applications [28, 34], the pipeline is focused on clean-looking rendering results but not clean geometry. To overcome this, several methods introduced additional con-

straints that focus on the geometric accuracy in the optimization. For example, the method of [16] restricts the variance to a 2D plane (the dimension of the surface). Another approach, SuGaR [15], extracts a mesh and realigns the Gaussian splats with the surface of this mesh to obtain a cleaner geometry. Gaussian opacity fields [35] combine Gaussians with a signed distance function to further regularize the results. While this leads to better geometry, the extraction of a mesh in the process is expensive and the extracted mesh might still be noisy. Without the extraction, outlier splats can prevail, and while they tend to not deteriorate the rendering, they can heavily interfere with geometry processing applications.

### 2.2. Laplacian-Beltrami Operator

**Laplacian Operator on Meshes.** The Laplace-Beltrami operator (LBO) is the generalization of the second derivative on general manifolds and a popular tool in many geometry processing applications. Its discretization, especially on triangular meshes, has been studied extensively and it has been shown that not all properties of the continuous Laplacian can be fulfilled in the discrete case at the same time [32]. While it is possible to use the graph Laplacian [31] on a mesh by discarding the face information, this fails to take into account all information about the local geometry. More advanced mesh LBOs, like the cotan discretization [20, 25] or intrinsic Delaunay discretization [5], provide a more accurate approximation of the continuous behaviour. These can also be extended to more complex domains, like n-dimensional data [12], general polygonal meshes [1, 7], or non-manifold meshes [29]. However, all of these depend on explicitly given connectivity information which can guarantee certain properties but does not work for less structured shape representations, like point clouds or Gaussian splatting.

**Laplacian Operator on Point Clouds.** As the discrete Laplacian operator relies on the definition of the neighborhood that is not explicitly given in the point cloud, it is essential to estimate the neighborhood function in a good way so that it approximate the intrinsic connectivity. A straight-forward solution would be to triangulate the point cloud, however, this is expensive and often leads to errors on sparse or noisy point clouds. Instead, a common solution is to *locally* approximate the surface via its tangent plane and projection of surrounding points onto it, often by a nearest neighbor search [4]. This works well on smooth or flat regions, but struggles around very sharp features. The resulting inaccuracies can be diminished by building an operator that is robust to incorrectly found and non-manifold surface connections [29], or by employing improvements in the surface estimation for these cases, for example through anisotropic Voronoi diagrams [26], or physic

dynamics [24]. The recent work of [23] avoids direct estimation of the surface by learning the behavior of the LBO on different examples and then generalizing the behavior directly to new point clouds. While the centers of a Gaussian splatting do form a point cloud on which the previous methods can be applied, the directional variance at each point provides valuable additional information about the surface. In this work we propose a more accurate way to extract the LBO from Gaussian splatting which includes the variances in the surface estimation.

### 3. Background

In this section we introduce the background on Gaussian splatting and the Laplace-Beltrami operator necessary to understand the rest of the paper.

#### 3.1. Gaussian Splatting

3D Gaussian splatting [19] represents a scene as a collection of 3D Gaussian distributions  $\{(\mu_i, \Sigma_i, \alpha_i, c_i)\}_i$  with mean  $\mu_i \in \mathbb{R}^3$ , variance  $\Sigma_i \in \mathbb{R}^{3 \times 3}$ , alpha value  $\alpha_i$ , and color function  $c_i$  in spherical harmonic representation. This collection can be easily projected to 2D and rendered by accumulating density along a ray. The parameters of each Gaussian splat are optimized to render to a set of training images from different view points. Since this optimization is focused on rendering, the 3D Gaussian splats are not necessarily localized on the surface of the objects in the scene. There have been efforts to align the 3D Gaussian splats to the surface by regularizing on the SDF [15], the depth and the normal [35], or training 2D Gaussian splatting [16], that focus on the geometry of the reconstructed mesh.

#### 3.2. (Discrete) Laplace-Beltrami Operator

The Laplace-Beltrami operator (LBO)  $L = \text{div} \cdot \nabla$  generalizes the second derivative to general closed compact manifolds. The operator and its eigenfunctions and eigenvalues, which are non-trivial solutions to  $L\phi_i = \lambda_i\phi_i$ , are popular tools in geometry processing (see Sec. 2.2). When discretizing the underlying manifold, the LBO also has to be discretized which leads to approximation artifacts [32].

The cotan-discretization [25] for triangular meshes is defined as follows:

$$W_{ij} = \begin{cases} \frac{1}{2}(\cot\alpha_{ij} + \cot\beta_{ij}), & \text{if } (i, j) \in E \\ -\sum_{k \in \mathcal{N}(i)} w_{ik}, & \text{if } j = i \\ 0, & \text{otherwise} \end{cases} \quad (1)$$

where  $\alpha_{ij}, \beta_{ij}$  are the opposing angles to the edge between vertices  $v_i, v_j$  (see Fig. 2). In combination with the diagonal mass matrix  $M$  describing the local weight at each vertex  $M_{ii}$  the area of the voronoi cell around vertex  $i$ , the LBO is  $L = M^{-1}W$ . While the default cotan-Laplacian does not fulfill the maximum principle, it will when applied to

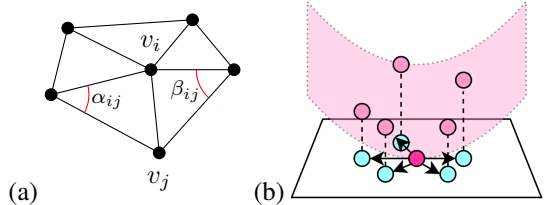


Figure 2. Discretization of the Laplace Beltrami operator on a mesh (a) and a point cloud (b). In the mesh the connectivity is directly given and can be used to compute properties like angles. The point cloud Laplacian relies on an approximation of tangent plane at a point on which the neighborhood is projected (blue).

the intrinsic Delaunay triangulation of the input mesh [5]. However, this depends on a clean mesh with only triangles and no non-manifoldness (e.g., edges with three triangles attached). For meshes of arbitrary topology, [29] suggested to use the tufted cover, which generates an implicit manifold overlay of a given connectivity, in combination with the intrinsic triangulation. Due to its flexibility w.r.t. the connectivity, the tufted Laplacian is also well-suited to be used on point clouds by approximating a local neighborhood and connectivity for each point without the need to reconstruct a full, consistent triangle mesh, which is expensive and prone to be noisy.

### 4. Method

We propose a discretization of the Laplace-Beltrami operator (LBO) that takes into account all geometric information that is given in Gaussian splatting and can serve as a quality measure for the surface information at the same time. As detailed in Sec. 3.2, the LBO encodes the local surface information so the main challenge is to construct the local neighborhood accurately, even though a collection of Gaussians has no explicit notion of connectivity. We explain how to do this in Sec. 4.1. The second challenge is that most Gaussian splatting is optimized to render well and not as an accurate geometry representation. Methods like 2D Gaussians [16] or SuGaR [15] aim to find a representation more localized on the surface but still contain many low-variance outliers. In Sec. 4.2 we explain how the properties of the LBO can be used to determine if a geometrically converged representation was found and how to use this during training.

#### 4.1. Local Neighborhood Construction

Gaussian splatting can be considered as a point cloud (the centers) with additional geometric information in form of a directional variance attached to each point. A straightforward implementation of the LBO could just apply the point cloud Laplacian [29] to the center point cloud, however, this ignores valuable information that the variance

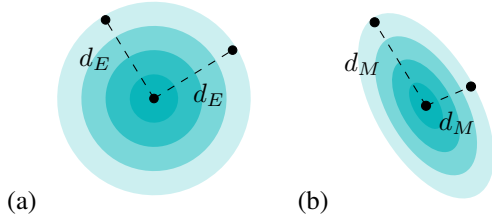


Figure 3. Difference between the (a) Euclidean distance and (b) Mahalanobis distance. In (a) and (b) the marked points both have the same distance to the center, however, in the Euclidean and Mahalanobis distances, respectively. The Mahalanobis distance allows weighting directions differently, which we do in our methods using the variance of the Gaussians.

gives. Instead of using the Euclidean neighborhood to estimate the local connectivity of the surface, we propose to use the Mahalanobis distance which can take into account the full Gaussian distribution present.

**Mahalanobis Distance.** The Mahalanobis distance is a measure of the distance between a point and a distribution  $\mathcal{G}$  with mean  $\mu \in \mathbb{R}^d$  and covariance  $\Sigma \in \mathbb{R}^{d \times d}$ . We only consider  $d = 3$  in this paper. It is defined as

$$d_M(p, \mathcal{G}) = \sqrt{(p - \mu)^T \Sigma^{-1} (p - \mu)}$$

for a point  $p \in \mathbb{R}^d$ . See Fig. 3 for a visualization. Intuitively, Gaussian splats have a higher variance along the tangent directions of the surface, and a low variance in normal direction. Thus, a neighborhood based on the Mahalanobis distance clusters together points that lie along side on the surface and give outliers a very high distance.

However, we can only compute the distance between a *point* and a distribution, but all elements of a Gaussian splatting are distributions. Computing the distance between two distributions, which is what we actually want, is possible, for example with the earth mover’s distance but computationally very expensive. In practice, we approximate by taking a symmetric approach and building neighborhoods between splats where edge points are both their respective Mahalanobis neighbors.

**Gaussian Laplacian.** The point cloud Laplacian requires a neighborhood  $\mathcal{N}_v$  of  $k$  nearest neighbors to be defined for each vertex  $v$  which is then used to approximate the local surface. Instead of computing the Euclidean nearest neighbors, we compute the following for each Gaussian center:  $(p_i, p_j)$  is an edge if  $p_i$  lies in the neighborhood of  $p_j$ , and  $p_j$  lies in the neighborhood of  $p_i$  using the  $k$ -nearest Mahalanobis neighbors. There can be multiple connected components in the constructed graph due to the existence of noisy Gaussian splats inside the objects. To filter out the Gaussian

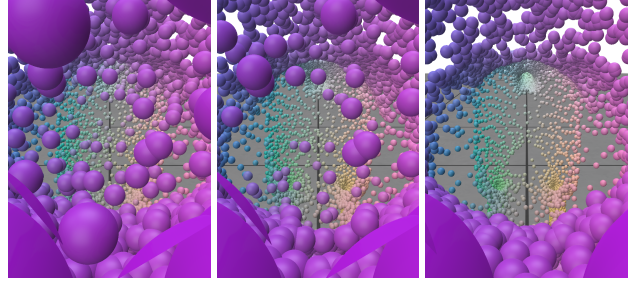


Figure 4. Example of the inside of the point cloud before(left), after (middle) filtering using the training from GOF [35], and using adaptive training (right).

splats that do not align to the surface, we take the largest connected component to be the final graph representation of the object.

The Laplacian of the Gaussian splatting is computed in the same fashion as for the point cloud Laplacian [29]. The point cloud is taken from the vertices of the constructed graph. Instead of computing the Euclidean distance, we construct the  $k$  nearest neighbors in Mahalanobis distance. Additionally, the point normal estimation can be done by setting the normal of the point to be the eigenvector corresponding to the smallest eigenvalue of covariance matrix of its Gaussian distribution instead of estimating the normals from the coordinates of the neighborhood. This setup is applicable under the assumption that the 3D Gaussian splats are mostly flat and well aligned to the surface, which is achieved by previous methods such as SuGaR [15] and GOF [35]. As GOF is the SOTA approach to reconstruct the mesh with good geometry from 3D Gaussian splattings, we use GOF to train the 3D Gaussian splatting.

## 4.2. Gaussian filtering

The optimization of a set of Gaussian splats often leads to outliers that do not contribute to the geometry or rendering. The original Gaussian splatting [19] already proposed to regularly remove splats with near zero opacity due to their low information. When rendering a closed surface, splats on the inside will not be visible and thus can also take high variance forms without adding to the solution (but also not degrading it) but adding noise to the geometric information. We propose to use the same symmetric Mahalanobis neighborhood construction to filter out these noisy Gaussians by pruning splats that are not in the largest connected component. See Fig. 4 for a visualization of the effect of filtering.

## 4.3. Adaptive Training

In previous work, the Chamfer distance [16, 35] is mainly used to evaluate the quality of geometry for Gaussian splatting. However, it is originally designed to evaluate the similarity between point clouds and thus does not take surface



properties into account. To overcome this, we introduce the spectrum, i.e. the eigenvalues, of the Laplace-Beltrami operator as an evaluation metric. The eigenvalues are a global description of the geometry of a shape [27] and can even be used to some extent to recover its geometry (“hearing the shape of a drum”) [11]. Although the ground truth spectrum of the reconstructed shape is unknown, we can use the eigenvalues to check for convergence of geometric properties, in addition to PSNR that is commonly used in 3D Gaussian splatting training. Finally, the number of zero eigenvalues describes how many disconnected components an object has. Removing all except the  $k$  biggest disconnected components is an efficient tool to get rid of outliers when doing training.

## 5. Experiments

In this section we show the effectiveness of our method. We mainly compare against the robust point cloud Laplacian [29] as a baseline and use the mesh Laplacian as the ground-truth on data generated from a given mesh instead of renderings only (see Sec. 5.1). We show superior performance on the computation of heat diffusion and the derived geodesic distance (Sec. 5.2), shape matching (Sec. 5.3), and the adaptation of training the Gaussian splatting using the LBO for filtering (Sec. 5.4). All experiments were done on a NVIDIA RTX 4090 with 64 GB RAM.

### 5.1. Evaluations and Comparisons

**Dataset.** We build the dataset from TOSCA [6] that provides 8 classes of non-rigid shapes with correspondence with at least 3 different poses in each class. We use blender to generate the image dataset for training, validation and testing. For each class we select 5 poses if any and generate 100 images of each shape for training, 50 images for validation and 30 images for testing. For simplicity, we down-scale the object by  $\frac{1}{20}$  before capturing the images to fit into a default camera frame. In comparison to other common 3DGS datasets such as Mip-NeRF360 [2], TOSCA contains meshes well-suited for geometry processing applications and a clean ground-truth mesh which we can use to quantitatively evaluate our method. We will publish this dataset with reconstructed 3DGS from TOSCA and correspondences between both with this paper to allow better evaluation of geometry processing applications on 3DGS.

**Evaluation Metrics.** The LBO matrices of different 3D representations cannot be compared directly because the discretization can vary significantly. We will use the eigenvalues and selected functions on the surface for comparing the performance of different approaches. The discretization differences also exist for these functions but the function values can be more easily projected onto a different dis-

cretization. In order to compare, we assume the smoothness of the functions between the existing samples and then project each vertex of the ground truth mesh onto the other representations (point cloud, 3D Gaussians, mesh from GOF) by distance. For each representation, we denote this correspondence by  $I$ .

**Eigenfunctions.** For the eigenvalues, the paper of [3] shows the convergence of the Laplacian operator in the spectrum regime. The eigenfunctions of the point cloud Laplacian converges to the eigenfunctions of the Laplacian-Beltrami operator in the underlying manifold in  $L_2$  norm with improved sampling. Thus, we propose to compare the eigenvalues and the eigenfunctions of the normalized Laplacian matrix, that is to solve  $Lx = \lambda Mx$  and compute the first  $K = 100$  eigenvalues (the lower the more stable) for all experiments. Since the eigenvalue is inversely proportional to the scale of the surface area, we calculate the normalized difference  $S|\lambda_i - \lambda_i^{gt}|$  for  $i = 1, \dots, 100$  for comparing eigenvalues. For the eigenfunctions, we apply the  $l_2$  metric and the normalized  $l_2$  metric

$$L_2(f_1, f'_1) = \left\| \frac{f_1}{\|f_1\|_2} - \frac{f'_1}{\|f'_1\|_2} \right\|_2$$

$$L_2^w(f_1, f'_1) = \left\| \frac{f_1}{\|f_1\|_w} - \frac{f'_1}{\|f'_1\|_w} \right\|_w$$

where  $\|f\|_w = f^T M f$  and  $M$  is the mass matrix of the ground truth mesh and  $f'$  the eigenfunction of a different representation projected onto the ground-truth mesh.

**Other Functions.** We apply the same projection before any comparisons also for the heat diffusion, geodesic distance and matching errors. We are able to compute the losses  $L_2(f(I), f_{gt})$  and  $L_2^w(f(I), f_{gt})$  of the respective functions.

**Comparisons** We compare our method to the following baselines since there are no targeted competitors for LBO on Gaussian splatting:

- **Point Cloud:** the point cloud Laplacian on the point cloud computed from centers of the 3D Gaussian splats,
- **Mesh (GOF):** reconstructing the mesh from a 3DGS using the SOTA approach of Gaussian opacity fields [35],
- **Ours (Euclid):** our GS Laplacian using the k-nearest neighbors in Euclidean distance to compute the normal direction (as in [29]), applied on the 3DGS filtered,
- **Ours (M+normal):** our GS Laplacian using the lowest magnitude variance direction as normal direction and using the k-nearest neighbors in Mahalanobis distance, applied on the 3DGS filtered,
- **Ours(AT+M+normal):** our GS Laplacian using the lowest magnitude variance direction as normal direction and using the k-nearest neighbors in Mahalanobis distance, applied on the 3DGS after adaptive training.

The ground-truth Laplace-Beltrami operator is computed from the ground-truth meshes (if given), and we use the

state-of-the-art approach [29] to compute the Laplacian operator on both point clouds, meshes and our adaption (also see Sec. 3.2).

## 5.2. Function Comparison

Since the LBO matrix itself is not directly comparable (see Sec. 5.1), we compare descriptive functions on the surface of each representation. We choose (i) the eigenfunctions of the LBO, (ii) heat diffusion applied from a collection of source points, and (iii) the geodesic distance computed using Geodesics in Heat [13].

**Eigenfunctions.** We take the first 10 eigenfunctions computed from each Laplace operator and compare their values to the eigenfunctions from the LBO on the ground-truth mesh in TOSCA. Tab. 1 shows the average over these 10 eigenfunctions for each class and operator. Our method and Mesh (GOF) perform on-par while both are much better than the point cloud Laplacian. However, Mesh (GOF) requires an extra step to extract a (very high resolution) mesh from the Gaussian splatting which is expensive to compute while our methods operates directly on the given data.

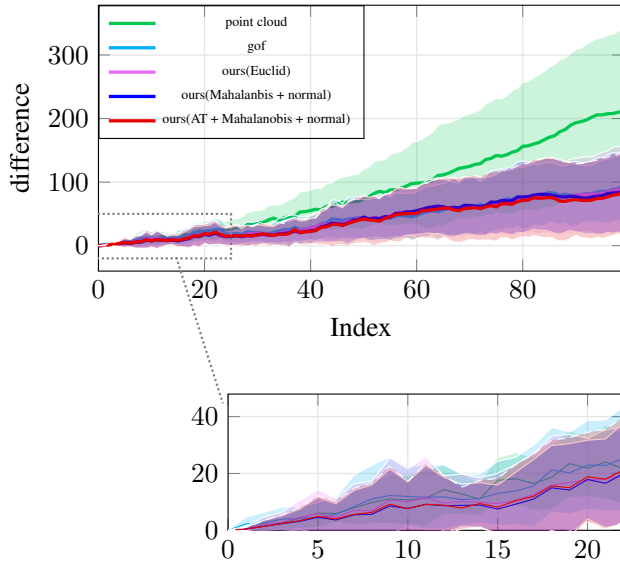


Figure 5. Statistical analysis over all the objects on the loss of eigenvalues. The index represents the order of the eigenvalue by magnitude. The line represent the average of the loss and one std is used for the confidence interval.

**Curvature** As an intrinsic property, the mean curvature can be derived from the Laplace-Beltrami operator via the equation  $\Delta p = -2Hn$ , where  $p$  denotes the coordinates,  $H$  the mean curvature and  $n$  the normal. This property can be used to evaluate the quality of the Laplacian Beltrami operator. We report qualitative and quantitative results in

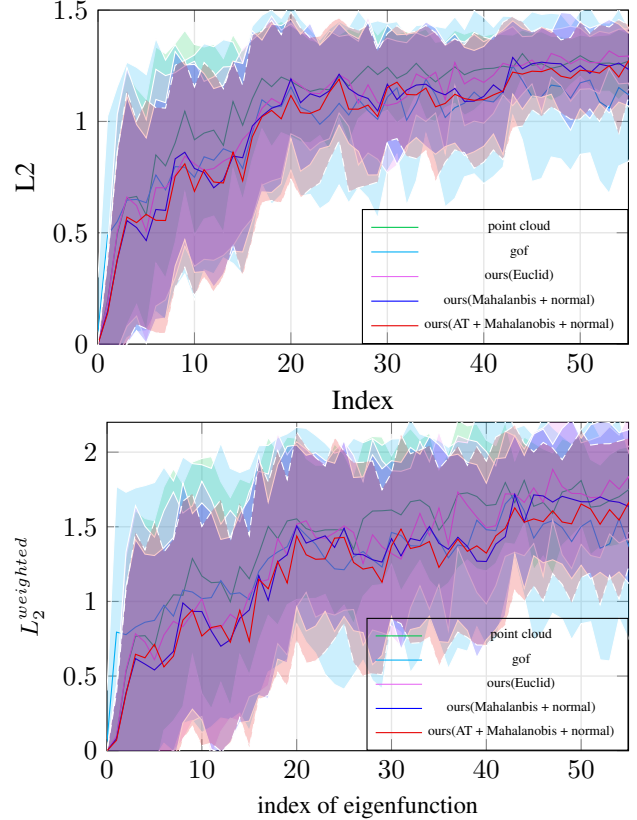


Figure 6. Statistical analysis of (weighted) loss on the eigenfunctions over all the objects. The index represents the order of the eigenvalue by magnitude. The line represent the average of the loss and one std is used for the confidence interval.



Figure 7. The mean curvature computed from the Laplacian operator. From left to right: ground truth curvature, curvature on the extracted mesh, curvature on 3DGS. Higher value represents larger mean curvature(absolute value). The extracted mesh contains many small artifacts manifested in the noise of the computed curvature. Our method is more similar to the ground truth.

Fig. 7 and Tab. 2. It turns out that our Laplacian is much closer to the ground truth mesh curvature than the curvature computed with the Laplacian on a mesh extracted from the 3DGS. The large discrepancy stems from the artifacts on the extracted mesh.

**Geodesic Distance** The geodesic distance represents the shortest path between two points on a surface, or more gen-

Class	#Num	Point Cloud		Mesh (GOF)		Ours (Euclid)		Ours (M+normal)		Ours (AT+M+normal)	
		$L_2$	$L_2^w$	$L_2$	$L_2^w$	$L_2$	$L_2^w$	$L_2$	$L_2^w$	$L_2$	$L_2^w$
Cat	5	0.529	0.546	0.383	0.423	0.392	0.386	0.409	0.342	<b>0.340</b>	<b>0.268</b>
Centaur	4	0.610	0.669	0.842	1.285	0.488	0.490	<b>0.479</b>	<b>0.496</b>	0.485	0.523
David	5	0.410	0.443	0.493	0.642	<b>0.338</b>	<b>0.312</b>	0.360	0.387	0.357	0.400
Dog	3	0.632	0.682	0.506	0.537	0.497	0.504	<b>0.470</b>	<b>0.445</b>	0.547	0.582
Horse	3	0.800	0.949	1.230	1.783	0.786	0.926	<b>0.773</b>	0.884	0.776	<b>0.846</b>
Michael	5	0.709	0.949	0.796	1.140	0.617	0.838	0.605	0.779	<b>0.589</b>	<b>0.767</b>
Victoria	5	0.909	1.131	<b>0.593</b>	<b>0.791</b>	0.917	1.159	0.685	0.861	0.680	0.861
Wolf	3	0.300	0.259	<b>0.043</b>	<b>0.002</b>	0.106	0.017	0.087	0.011	0.135	0.032
Total	33	0.619	0.718	0.607	0.821	0.528	0.599	<b>0.491</b>	<b>0.541</b>	<b>0.489</b>	<b>0.544</b>

Table 1.  $L_2$  distance between eigenfunction of each operator and the ground-truth mesh eigenfunctions. See Sec. 5.1 for definition of the metrics. While Mesh (GOF) and our method perform on-par, our method does not require the extraction of a mesh.

Type	Mesh(GOF)	Point Cloud	Ours(M+normal)	Ours(AT+M+normal)
Avg	43.049	17.746	16.317	<b>16.023</b>
Min	12.720	7.954	6.332	<b>6.202</b>
Max	129.369	33.621	29.867	<b>29.306</b>

Table 2.  $L_1$ -error of the mean curvature computed from the Laplacian operator on an extracted mesh, point cloud, ours with Mahalanobis distance and ours with adaptive training.

erally a Riemannian manifold. We use the exact "single source, all destination" algorithm proposed by Michell et al. [21] to compute the distance on the ground-truth meshes. For non-mesh data structures, Crane et al.[13] proposed the heat method to approximate the distance using the Laplace operator on any domain that allows the computation of gradient and divergence.

For each object, we uniformly sample 100 sources and compute the mean of the errors as

$$\mathcal{E}_{geo}(\Delta) = \frac{1}{100} \frac{1}{\sqrt{S}} \sum_{i=1}^{100} \sum_{j=1}^N |d^j - d_{\Delta}^j|$$

where  $S$  is the surface area,  $N$  is the number of points of the ground-truth mesh,  $d^j$  is the exact geodesic distance [21] from the point  $j$  to the source point and  $d_{\Delta}^j$  is the geodesic distance from  $j$  to the source point using the LBO  $\Delta$ .

Sec. 5.2 shows the comparison of geodesic distance errors. All methods are computed using Geodesics in Heat and compared to the exact distance. The Mesh (GT) column is given as a reference to see the error induced by the Geodesics in Heat, not as a direct competitor as the ground truth mesh is not known in practice. Our method is as good as and often better than the mesh reconstruction, and is much better than the center point cloud Laplacian.

### 5.3. Shape Matching

A fundamental problem in geometry processing is finding correspondences between pairs of non-rigid 3D shapes. The approach of functional maps [22] provides an efficient

Category	Mesh(GT)	Point Cloud	Mesh(GOF)	Ours(Euclid)	Ours(M+normal)	Ours(AT+M+normal)
Cat	0.017	0.045	0.028	0.034	0.027	<b>0.026</b>
Centaur	0.018	0.036	0.024	0.023	0.023	<b>0.022</b>
David	0.036	0.050	0.058	0.038	<b>0.035</b>	<b>0.035</b>
Dog	0.016	0.050	0.037	0.036	<b>0.031</b>	0.032
Horse	0.016	0.046	0.029	<b>0.022</b>	<b>0.022</b>	<b>0.022</b>
Michael	0.038	0.051	0.065	<b>0.046</b>	0.047	<b>0.046</b>
Victoria	0.035	0.117	<b>0.078</b>	0.113	0.095	0.082
Wolf	0.012	0.036	<b>0.010</b>	0.017	0.018	0.018
Total	0.025	0.056	0.045	0.045	0.040	<b>0.038</b>

Table 3. Average error in geodesic computation  $\mathcal{E}_{geo}$  by heat method [13] in comparison to the exact distance on the ground-truth mesh. The bold represents the best score and the gray represents the second best.

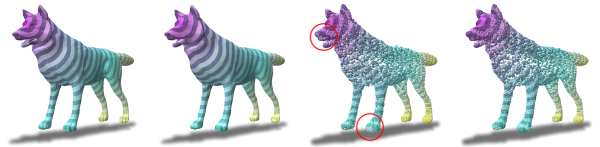


Figure 8. Geodesics in Heat [13] computed on (from left to right) the ground-truth mesh, the reconstructed mesh (GOF), the center point cloud (unfiltered) and the filtered Gaussian splatting (ours). The filtering significantly improves the results (see red circles).

framework to compute these in functional space where the Laplace-Beltrami basis is used for dimensionality reduction. We will use this application to show the effectiveness of our Laplace-Beltrami operator on 3DGS by comparing accuracy in representing correspondences. Given the ground-truth correspondence in form of a permutation  $P$ , it can be projected into functional map representation by taking

$$C = \Phi_t^T M_t P \Phi_s \quad (2)$$

where  $\Phi$  is the matrix of the first (ordered by frequency)  $k$  stacked eigenvectors of the source and target shape, respectively, and  $M_t$  the mass matrix on the target shape. A correspondence  $\text{Corr}_{(s,t)}$  can be extracted by taking nearest neighbors in the aligned spectral space between the points in  $\Phi_t$  and  $C\Phi_s$ . Since we do not want to evaluate a specific matching algorithm, this projection of the ground-

truth, which still leads to errors due to the dimension reduction, gives us a measure of the quality of the eigenbasis used, and in turn of our Laplace Beltrami operator.

For computational reasons, we use  $k = 100$  eigenfunctions and uniformly sample 1000 vertices to compute the geodesic error. We do the experiments on the TOSCA dataset. Since the vertices on the meshes are different from those derived from the 3D Gaussians, we are only able to compute the approximate geodesic error

$$\begin{aligned} q^{gt} &= \text{Corr}_{gt}(p^s) \\ q^\Delta &= P_{pc \rightarrow m}^t \text{Corr}_{(s,t)}(P_{m \rightarrow pc}^s p^s) \\ \mathcal{E}_{corr}^{(s,t)}(p^s) &= \frac{1}{\sqrt{S^t}} \text{dist}(q^{gt}, q^\Delta) \end{aligned}$$

where  $p^s$  is a vertex on the mesh of the source object,  $P_{pc \rightarrow m}^t$  denotes the projection from the point cloud derived from 3D Gaussians to the mesh of the target object and  $P_{m \rightarrow pc}^s$  denotes the projection from the mesh of the source object to the point cloud of the source object.  $\text{Corr}_{(s,t)}$  is the point-wise correspondence from the source object to the target object computed using the eigenfunction of  $\Delta^s$  and  $\Delta^t$  [22] as described above. While extracting the mesh via GOF performs slightly better, our method outperforms the point cloud Laplacian as visible in Fig. 9 and Fig. 10.

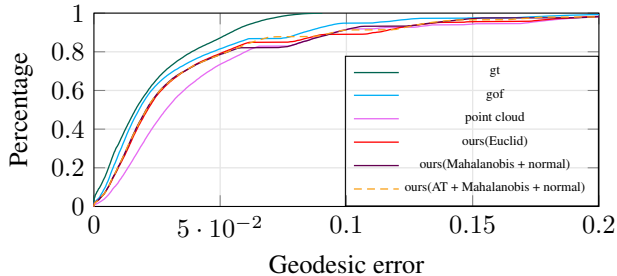


Figure 9. Geodesic error representing the ground-truth correspondence in a low-dimensional LBO basis, averaged over all the categories. For each category, we take a loop to select the pairs. For example, centaur0→centaur2, centaur2→centaur3, centaur3→centaur4, centaur4→centaur0 are selected pairs in the centaur category. The line represent the average of the error.

#### 5.4. Adaptive Training of 3DGS

We use our adaptive training technique (Sec. 4.3) and point cloud filtering (Sec. 4.2) to improve the geometry of the results when training 3DGS. Specifically, we filter every  $N = 2000$  iterations and remove all except the  $k = 1$  biggest components at the same time. Note that finding all the connected components can be achieved by breadth-first search in complexity  $O(N)$ , hence the extra cost of computation is insignificant during training.

Remarkably, this training scheme leads to a very clean geometry with nearly no outlier splats in the geometry (see

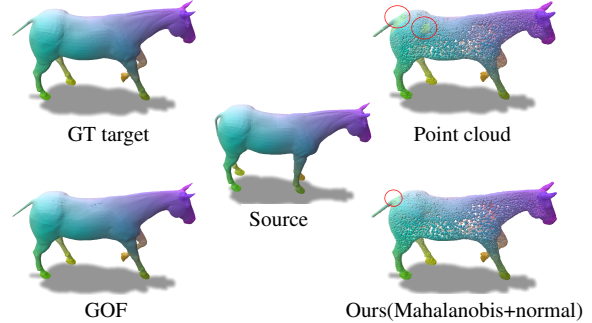


Figure 10. Color map for shape matching in the horse category. The source map (center) is colored by coordinate and the colors transferred with the correspondence computed by each method to the surrounding shapes. Inconsistencies in color indicate problems with the correspondence.

Category	Mesh (GT)	GOF training	Mesh (GOF)	Graph filtration (ours)	Adaptive training
Cat	27894	15522	157639	14005	<b>10701</b>
Centaur	<b>15768</b>	24792	248178	22769	18556
David	52565	17822	184600	16389	<b>13468</b>
Dog	25290	13066	142177	12088	<b>10479</b>
Horse	19248	39442	382236	35891	<b>28686</b>
Michael	52565	16762	174251	15432	<b>13431</b>
Victoria	45659	14560	146665	13330	<b>10922</b>
Wolf	<b>4344</b>	13188	143172	12202	9943

Table 4. Comparison of the size of different representations. For the mesh we report the number of vertices. For 3D Gaussian splatting we report the number of 3D Gaussian splats.

Fig. 4). It achieves on-par performance with other versions of our method and mesh reconstruction method in the comparison of eigenfunctions in Tab. 1 and a slightly closer spectrum to the ground truth as visible in in Fig. 5. In addition to having the best geometry in the sense of the spectrum of Laplacian operator, the adaptive training produces a much more compact representation (in terms of number of points) compared to the reconstructed meshes, the 3D Gaussian splats from GOF, the filtered 3D Gaussian splats, and even the original meshes.

During the training of 3D Gaussian splatting, we can also monitor the behavior of the spectrum of the Laplacian operator. We found that PSNR does not capture geometric information well. This can be seen from the different convergence behavior of PSNR and the first 8 eigenvalues in Fig. 11. PSNR converges around iteration 12k while the geometry stabilizes at the iteration 22k. Thus, the spectrum can be used as an augmenting measure to check the stabilization of the geometry during training.

#### 6. Geometry Smoothing

As an additional experiment from the area of geometry processing, we show how the optimized geometry can be manipulated easily with the LBO operator. We compute the LBO on the 3DGS and use the first 500 eigenfunctions to form a low frequency function space, denoted by



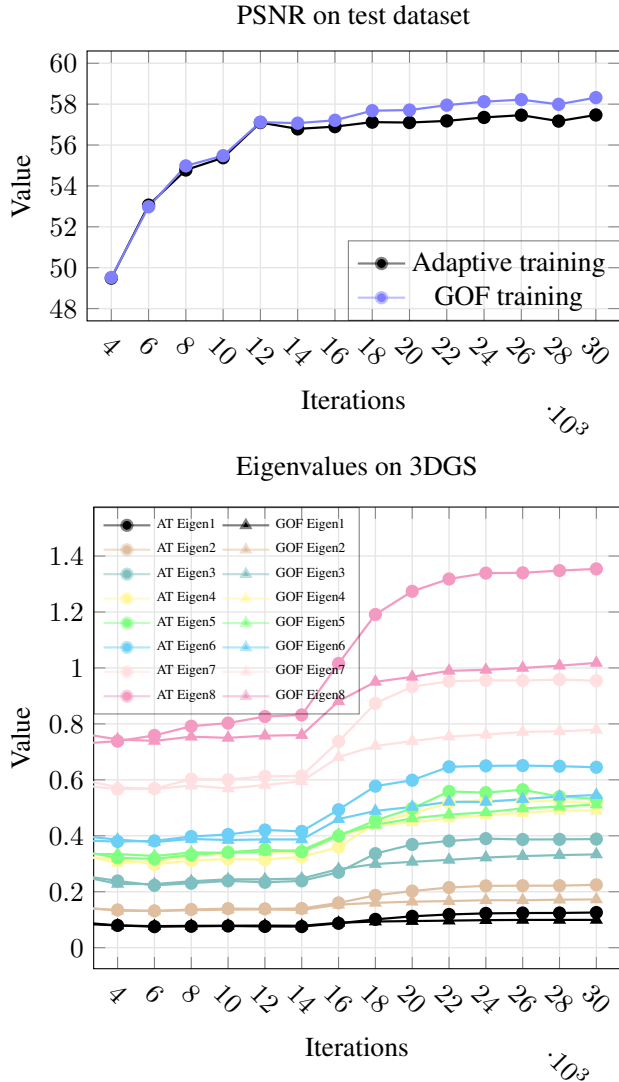


Figure 11. Evaluation metrics of PSNR (top) and spectrum (bottom) during training.

$\phi \in \mathbb{R}^{n \times 500}$ . Then, we project the xyz-coordinate functions onto  $\phi$  to perform a low pass filtering (smoothing):

$$v = \phi \phi^T M v, v \in \{x, y, z\},$$

where  $M$  is the mass matrix. We show the results using  $k = 500$  on the chair shape in Fig. 1 where even view dependent lighting effects are preserved under this smoothing operation.

## 7. Conclusion

We defined a new Laplace Beltrami operator that can be directly computed on 3D Gaussian splatting by using the Mahalanobis distance on the Gaussian splats using the variance to determine the neighborhood and filter out outlier

splats. Our experiments show that this performs much better than just computing the point cloud Laplacian on the point cloud of Gaussian centers, and also does not require an extra expensive step like extracting a mesh from the 3D Gaussians. Additionally, while an extracted mesh can lead to accurate computations, the mesh might also contain topological noise (e.g. in the form of disconnected components) which distorts the results significantly. Our Laplacian allows common geometry processing applications, like shape matching, to be directly performed on 3DGS, and the GS Laplacian can be used during training to determine convergence and improve the quality of the geometry.

## References

- [1] Marc Alexa and Max Wardetzky. Discrete laplacians on general polygonal meshes. *ACM Trans. Graph.*, 30(4), 2011. 2
- [2] Jonathan T Barron, Ben Mildenhall, Dor Verbin, Pratul P Srinivasan, and Peter Hedman. Mip-nerf 360: Unbounded anti-aliased neural radiance fields. In *Proceedings of the IEEE/CVF conference on computer vision and pattern recognition*, pages 5470–5479, 2022. 1, 5
- [3] Mikhail Belkin and Partha Niyogi. Convergence of laplacian eigenmaps. *Advances in neural information processing systems*, 19, 2006. 5
- [4] Mikhail Belkin, Jian Sun, and Yusu Wang. Constructing laplace operator from point clouds in rd. In *ACM-SIAM Symposium on Discrete Algorithms*, 2009. 2
- [5] Alexander I. Bobenko and Boris A. Springborn. A discrete laplace-beltrami operator for simplicial surfaces. *Disc. & Comp. Geom.*, 38(4), 2007. 2, 3
- [6] Alex M. Bronstein, Michael M. Bronstein, and Ron Kimmel. *Numerical Geometry of Non-Rigid Shapes*. Springer, 2008. 2, 5
- [7] Astrid Bunge, Philipp Herholz, Misha Kazhdan, and Mario Botsch. Polygon laplacian made simple. *Computer Graphics Forum*, 39(2), 2020. 2
- [8] Jiazhong Cen, Jiemin Fang, Chen Yang, Lingxi Xie, Xiaopeng Zhang, Wei Shen, and Qi Tian. Segment any 3d gaussians. *arXiv preprint arXiv:2312.00860*, 2023. 1
- [9] Guikun Chen and Wenguan Wang. A survey on 3d gaussian splatting, 2024. 2
- [10] Hanlin Chen, Chen Li, and Gim Hee Lee. Neusg: Neural implicit surface reconstruction with 3d gaussian splatting guidance, 2023. 1
- [11] Luca Cosmo, Mikhail Panine, Arianna Rampini, Maks Ovsjanikov, Michael M. Bronstein, and Rodola Rodola. Isospectralization, or how to hear shape, style, and correspondence. In *Proceedings - 2019 IEEE/CVF Conference on Computer Vision and Pattern Recognition, CVPR 2019*, pages 7521–7530, 2019. 5
- [12] Keenan Crane. The n-dimensional cotangent formula. Technical report, Carnegie Mellon University, 2019. 2
- [13] Keenan Crane, Clarisse Weischedel, and Max Wardetzky. The heat method for distance computation. *Communications of the ACM*, 60(11):90–99, 2017. 6, 7

- [14] Lin Gao, Jie Yang, Botao Zhang, Jiamu Sun, Yujie Yuan, Hongbo Fu, and Yu-Kun Lai. Real-time large-scale deformation of gaussian splatting. *ACM Transactions on Graphics (SIGGRAPH Asia 2024)*, 2024. 1
- [15] Antoine Guédon and Vincent Lepetit. Sugar: Surface-aligned gaussian splatting for efficient 3d mesh reconstruction and high-quality mesh rendering. *CVPR*, 2024. 1, 2, 3, 4
- [16] Binbin Huang, Zehao Yu, Anpei Chen, Andreas Geiger, and Shenghua Gao. 2d gaussian splatting for geometrically accurate radiance fields. In *SIGGRAPH 2024 Conference Papers*. Association for Computing Machinery, 2024. 1, 2, 3, 4
- [17] Yi-Hua Huang, Yang-Tian Sun, Ziyi Yang, Xiaoyang Lyu, Yan-Pei Cao, and Xiaojuan Qi. Sc-gs: Sparse-controlled gaussian splatting for editable dynamic scenes. *CVPR*, 2024. 1
- [18] Michael Kazhdan, Matthew Bolitho, and Hugues Hoppe. Poisson surface reconstruction. In *Proceedings of the Fourth Eurographics Symposium on Geometry Processing*. Eurographics Association, 2006. 1
- [19] Bernhard Kerbl, Georgios Kopanas, Thomas Leimkühler, and George Drettakis. 3d gaussian splatting for real-time radiance field rendering. *ACM Transactions on Graphics*, 42(4), 2023. 1, 2, 3, 4
- [20] Mark Meyer, Mathieu Desbrun, Peter Schröder, and Alan H. Barr. Discrete differential-geometry operators for triangulated 2-manifolds. In *Visualization and Mathematics III*, 2003. 2
- [21] Joseph SB Mitchell, David M Mount, and Christos H Papadimitriou. The discrete geodesic problem. *SIAM Journal on Computing*, 16(4):647–668, 1987. 7
- [22] Maks Ovsjanikov, Mirela Ben-Chen, Justin Solomon, Adrian Butscher, and Leonidas Guibas. Functional maps: a flexible representation of maps between shapes. *ACM Transactions on Graphics (ToG)*, 31(4):1–11, 2012. 2, 7, 8
- [23] Bo Pang, Zhongtian Zheng, Yilong Li, Guoping Wang, and Peng-Shuai Wang. Neural laplacian operator for 3d point clouds, 2024. 3
- [24] F. Petronetto, A. Paiva, E. S. Helou, D. E. Stewart, and L. G. Nonato. Mesh-free discrete laplace–beltrami operator. *Computer Graphics Forum*, 32(6), 2013. 3
- [25] Ulrich Pinkall and Konrad Porthier. Computing discrete minimal surfaces and their conjugates. *Experim. Math.*, 1993. 2, 3
- [26] Hongxing Qin, Yi Chen, Yunhai Wang, Xiaoyang Hong, Kangkang Yin, and Hui Huang. Laplace–beltrami operator on point clouds based on anisotropic voronoi diagram. *Computer Graphics Forum*, 37(6), 2018. 2
- [27] Martin Reuter, Franz-Erich Wolter, and Niklas Peinecke. Laplace–beltrami spectra as ‘shape-dna’ of surfaces and solids. *Computer-Aided Design*, 38(4):342–366, 2006. Symposium on Solid and Physical Modeling 2005. 5
- [28] Zhijing Shao, Zhaolong Wang, Zhuang Li, Duotun Wang, Xiangru Lin, Yu Zhang, Mingming Fan, and Zeyu Wang. SplattingAvatar: Realistic Real-Time Human Avatars with Mesh-Embedded Gaussian Splatting. In *Computer Vision and Pattern Recognition (CVPR)*, 2024. 2
- [29] Nicholas Sharp and Keenan Crane. A laplacian for nonmanifold triangle meshes. *Computer Graphics Forum (CGF)*, 2020. 2, 3, 4, 5, 6
- [30] Olga Sorkine. Laplacian Mesh Processing. In *Eurographics*, 2005. 2
- [31] Gabriel Taubin. A signal processing approach to fair surface design. In *SIGGRAPH*, 1995. 2
- [32] Max Wardetzky, Saurabh Mathur, Felix Kälberer, and Eitan Grinspun. Discrete laplace operators: No free lunch. In *Proc. of Eurographics Symposium on Geometry Processing (SGP)*, 2007. 2, 3
- [33] Simon Weber, Thomas Dages, Maolin Gao, and Daniel Cremers. Finsler-laplace-beltrami operators with application to shape analysis. In *2024 IEEE/CVF Conference on Computer Vision and Pattern Recognition (CVPR)*, pages 3131–3140, 2024. 2
- [34] Yunzhi Yan, Haotong Lin, Chenxu Zhou, Weijie Wang, Haiyang Sun, Kun Zhan, Xianpeng Lang, Xiaowei Zhou, and Sida Peng. Street gaussians for modeling dynamic urban scenes. In *ECCV*, 2024. 2
- [35] Zehao Yu, Torsten Sattler, and Andreas Geiger. Gaussian opacity fields: Efficient and compact surface reconstruction in unbounded scenes. *arXiv preprint arXiv:2404.10772*, 2024. 2, 3, 4, 5